Switching on thermal and light-induced spin crossover by desolvation of [Fe(3-bpp)2](XO4)2×solvent (X = Cl, Re) compounds

Abdelhak Djemel, Olaf Stefanczyk, Cédric Desplanches, Kunal Kumar, Rachid Delimi, Farouk Benaceur, Shin-Ichi Ohkoshi, Guillaume Chastanet

Switching on thermal and light-induced spin crossover by desolvation of $[Fe(3\text{-bpp})_2](XO_4)_2\cdot$solvent (X = Cl, Re) compounds†

Abdelhak Djemel[ab], Olaf Stefanczyk*[ac], Cédric Desplanches[a], Kunal Kumar[c], Rachid Delimi[d], Farouk Benaceur[b], Shin-ichi Ohkoshi[c] and Guillaume Chastanet *[a]

[a]*CNRS, Univ. Bordeaux, Bordeaux INP, ICMCB, UMR 5026, 87 avenue du Dr A. Schweitzer, Pessac, F-33608, France.* E-mail: guillaume.chastanet@icmcb.cnrs.fr
[b]*Research Unit of Medicinal Plants (RUMP), University Pole No 02, Laghouat 03000, attached to Biotechnology Research Center (CRBt), BP E73 Ali Mendjeli, Constantine 25000, Algeria*
[c]*Department of Chemistry, School of Science, The University of Tokyo, 7-3-1 Hongo, Bunkyo-ku, Tokyo 113-0033, Japan.* E-mail: olaf@chem.s.u-tokyo.ac.jp
[d]*Badji Mokhtar University Annaba, Laboratory of Water Treatment and Valorization of Industrial Wastes, BP 12, Annaba 23000, Algeria*

Footnote : † Electronic supplementary information (ESI) available: Thermogravimetric analyses, pictures of samples, UV-Vis-NIR and IR spectroscopy, computation details, single-crystal and powder X-ray diffraction studies, and photomagnetic data. CCDC 2073012 and 2073013. For ESI and crystallographic data in CIF or other electronic format see DOI: 10.1039/d1qi00446h

Abstract : Thermal desolvation is a very attractive method for the post-synthetic modification of the physicochemical properties of switchable materials. In this field of research, special attention has been paid to the possibility of modifying the thermo- and photo-induced spin crossover (SCO) properties of metal complexes as they can act as solvent sensors. Two new $[Fe(3\text{-bpp})_2](ClO_4)_2\cdot 2.5H_2O\cdot MeOH$ (**1·sol**) and $[Fe(3\text{-bpp})_2](ReO_4)_2\cdot 3H_2O$ (**2·sol**) compounds, where 3-bpp is 2,6-di-(1*H*-pyrazol-3-yl)pyridine, were prepared and structurally characterized, and their solvated and desolvated phases were additionally investigated spectroscopically, magnetically and photomagnetically. Single-crystal X-ray structures of **1·sol** and **2·sol** consist of similar $[Fe(3\text{-bpp})_2]^{2+}$ units arranged in π–π stacked layers separated by H-bond-stabilised layers consisting of solvent molecules and anions. Moreover, both materials show desolvation-assisted SCO from a low (LS, S = 0) to high-spin state (HS, S = 2) at around 340 K, followed by a reversible gradual spin conversion with $T_{1/2}$ ≈ 210 K and 304 K for **1** and **2**, respectively. Photomagnetic studies of **1·sol** and **1** confirmed the efficiency of the light-induced excited spin-state trapping (LIESST) phenomenon with relaxation temperatures T(LIESST) = 82 K and 66 K for the solvated and desolvated phases, respectively. In the case of **2·sol**, no LIESST effect was observed while the desolvated phase **2** exhibits a LIESST behaviour at T(LIESST) ≈ 50 K.

Introduction

The research and development of molecular switchable materials is one of the major challenges in modern material chemistry due to their potential application in the construction of novel classes of data storage and processing devices and sophisticated sensors dedicated for specific applications.[1] In this respect, the molecular complexes exhibiting spin crossover (SCO) appear to be the closest to practical applications.[2] Typical SCO systems are based on pseudo–octahedral Fe(II) complexes ([Ar]3d^6). They are able to switch between a high-spin (HS) paramagnetic state with spin S = 2, and a low-spin (LS) diamagnetic state with spin S = 0, under the influence of external physical (temperature – T, pressure – P, magnetic field – H, light – hν) and chemical (chemical potential – μ, pH, absorption or desorption of host molecules) stimuli.[3] These switching processes not only lead to the alteration of their magnetic properties but also alter many other physical properties (*e.g.*,

optical properties, conductivity, and heat capacity).[4] It is worth pointing out that the spin crossover phenomenon is not exclusive for Fe(II) systems. In less common cases it can also be detected for other metal complexes with $3d^4$ (*i.e.* Cr(II), Mn(III)), $3d^5$ (*i.e.* Mn(II), Fe(III)), $3d^6$ (*i.e.* Co(III)), and $3d^7$ (*i.e.* Co(II), Ni(III)) configurations.[5]

To promote spin crossover at room temperature, many families of compounds have been explored such as the 0D-coordination complexes based on the bpp tridentate ligand (bpp being either 2,6-di-(1*H*-pyrazol-3-yl)pyridine (3-bpp) or 2,6-di-(1*H*-pyrazol-1-yl)pyridine (1-bpp)),[6] the 1D-coordination polymer based on triazole ligands[7] or the 2D and 3D-coordination networks of the Hoffman family.[3c] The main strategy followed in the design of these families was to favour strong intermolecular interactions in order to promote a cooperative character of the spin crossover at the origin of memory effects.[8] Apart from coordination polymers that intrinsically afford cooperative interactions within the coordination network, molecules able to promote hydrogen bonding or π–π stacking for instance are highly investigated.

Fe(II) complexes with the 3-bpp ligand are known to exhibit promising properties (e.g., near-room temperature transitions,[10–12] thermal hysteresis[9–11,13,14]) and solvent dependent behaviours.[10,12d,e,13a] Indeed, the cooperative and hysteretic transformation principally promoted by elastic interactions between complexes through weak interactions (van der Waals interactions, hydrogen bonds, π–π stacking), is strongly stimulated by the tris-heterocyclic *N*,*N*,*N*-tridentate 3-bpp ligand with several aromatic rings, ready to form π–π, anion–π_{ring} and $\sigma_{solvent}\cdots\pi_{ring}$ interactions, as well as up to four N_{ring}–H···X hydrogen bonds per one $[Fe(3\text{-bpp})_2]$. This finds practical confirmation in the observation of the 14 K-wide thermal hysteresis loop for $[Fe(3\text{-bpp})_2](triflate)_2\cdot H_2O$ for instance.[9]

For such $[Fe(3\text{-bpp})_2]^{2+}$ complexes, there are two main ways of modulating the intermolecular interactions network. The first one is the impact of solvation on spin crossover characteristics.[10,12d,e,13a] This stems from the fact that solvent molecules present in the crystal structures are deeply involved in the intermolecular interactions. Frequently, more cooperative transitions occur after desolvation; however, it comes with a significant decrease in the spin transition temperature ($T_{1/2}$) – the temperature at which half of the complex is in a LS state. For instance, $[Fe(3\text{-bpp})_2]I_2\cdot 4H_2O$ exhibits a gradual SCO at $T_{1/2} > 320$ K, the same material with two water molecules shows an abrupt SCO at $T_{1/2} = 256$ K, while the anhydrous one reveals an abrupt SCO at $T_{1/2} = 204$ K and narrow thermal hysteresis.[10] In the most extreme case, the pristine diamagnetic compound $[Fe(3\text{-bpp})_2](triflate)_2\cdot 3H_2O$, after the loss of two water molecules, exhibits an abrupt SCO with large thermal hysteresis ($T^{\downarrow}_{1/2} = 147$ K and $T^{\uparrow}_{1/2} = 285$ K).[9] A second way to tune the intermolecular interaction network is to vary the anions, also involved in the construction of such an intermolecular network. Up to now, more than 20 types of organic and inorganic anions have been applied in the syntheses of $[Fe(3\text{-bpp})_2]$ SCO systems.[9–19] This results in the following series of anions ordered according to increasing temperatures $T_{1/2}$ for the most solvated phases of Fe(II) complexes: $[Fe(CN)_5(NO)]^{2-}$ (183 K)[16] < BPh_4^- (ca. 200 K)[12c] < NCS^- (227 K)[10a,15d] ≈ $NCSe^-$ (230 K)[10a,15] ≈ $[Au(SCN)_2]^-$ (232 K)[12c] < $[Ag(CN)_2]^-$ (251 K)[12c] < BF_4^- (288 K)[10] ≈ $[Au(CN)_2]^-$ (291 K)[12c] < PF_6^- (ca. 300 K)[10b,12e] < ClO_4^- (above 313 K)[12e] < I^- (above 320 K)[10b] < Br^- (340 K)[10] < NO_3^- (ca. 350 K).[10b] From this series it can be concluded that the halides and oxygen-rich anions are the most promising counterions for the observation of room temperature SCO. However, above room temperature switching might also be promoted by a concomitant desolvation.[19] This desolvation also strongly impacts the lifetime of the photo-induced state. Indeed, in special cases, Fe(II) complexes can reveal a light-induced excited spin-state trapping (LIESST) effect – switching between the LS ground state and the metastable HS state after irradiation with light at low temperature, at which the metastable HS state exists long enough to be detected in the experiment.[20] The lifetime of the photo-induced state can be estimated through the measurement of the relaxation temperature *T*(LIESST).[21] This relaxation temperature is linked to $T_{1/2}$ according to the inverse energy gap law: if upon desolvation $T_{1/2}$ decreases therefore, *T*(LIESST) should increase.[10a]

As part of our long term study of such $[Fe(3\text{-bpp})_2]^{2+}$ complexes,[13,15] we focused on $[Fe(3\text{-bpp})_2](XO_4)_2\cdot S$ compounds with X = Cl and Re. The perchlorate-based compound showing gradual SCO above room temperature for the dehydrated phase has already been tested by Goodwin *et al.* in 1988,[12e] but magnetic data

need to be re-measured using more sophisticated equipment and missing structural, spectroscopic and photomagnetic data should be completed. Consequently, we decided to investigate this compound from the crystal structure, spectroscopic, magnetic and photomagnetic points of view, on the solvated and desolvated phases, and to compare its features to a newly synthesized perrhenate derivative.[22] This allowed us to determine the impact of anion substitution and desolvation on SCO and LIESST properties of these two compounds. As a result, we obtained and comprehensively characterised $[Fe(3\text{-bpp})_2](ClO_4)_2{\cdot}2.5H_2O{\cdot}MeOH$ (**1·sol**) and $[Fe(3\text{-bpp})_2](ReO_4)_2{\cdot}3H_2O$ (**2·sol**) and their desolvated phases which will be described in detail later in this work.

Results and discussion

Syntheses

The first preliminary attempts to obtain monocrystalline $[Fe(3\text{-bpp})_2](ClO_4)_2{\cdot}$solvent compounds were carried out by Sugiyarto and co-workers, using water as the solvent.[12e] Contrary to the previous method, in the present study, a methanolic solution of Fe(II) chloride and 3-bpp ligand was treated with an aqueous solution of $NaClO_4$, resulting in the formation of dark red prismatic crystals $[Fe(3\text{-bpp})_2](ClO_4)_2{\cdot}2.5H_2O{\cdot}MeOH$ (**1·sol**). The analogous synthesis, replacing $NaClO_4$ by $KReO_4$, yields dark red prismatic crystals of the $[Fe(3\text{-bpp})_2](ReO_4)_2{\cdot}3H_2O$ complex (**2·sol**). At this point, it is worth emphasizing the lack of chlorides in the final products, despite their presence in the mother liquors. This directly confirms a stronger affinity of the O-donor anions than the halogen-donor ones and the efficiency of the anion exchange, most likely thanks to the formation of stronger hydrogen bond interactions between 3-bpp ligands and anions (hydrogen bond acceptors).

Thermal stability, colour changes and spectroscopy

In order to determine the composition and thermal stability of both compounds, thermogravimetric analyses were performed in dry nitrogen flow on pristine samples **1·sol** and **2·sol** in the temperature range of 20–400 °C with stabilisation at 25 °C for 1 hour (ESI, Fig. S1†). After isothermal desolvation at 25 °C, **1·sol** loses half methanol and two water molecules (6.9% of the initial mass), and **2·sol** releases 1.25 water molecules (2.2% of the primary mass). A further increase in temperature resulted in the release of additional 1.5 water molecules from **1·sol** (3.6% of the original mass) at just above 54.5 °C and the loss of the residual two water molecules from **2·sol** (3.8% of initial mass) in two steps at 50.5 °C and 66 °C. Above 75 °C, **1·sol** and **2·sol** reach an anhydrous state $[Fe(3\text{-bpp})_2](XO_4)_2$ (X = Cl, **1** and Re, **2**). Next, both samples are stable up to 220 °C and 310 °C for **1** and **2**, respectively. Above these temperatures perchlorates and 3-bpp start to decompose. The total weight losses during desolvation are estimated to be around 10.5% and 6.0%, which correspond to the release of approximately 0.5 MeOH and 3.5 H_2O for **1·sol** and 3.25 H_2O for **2·sol**. These values are slightly different from those estimated on the basis of elemental analysis (1 MeOH and 1.75 H_2O for **1·sol** and 2.5 H_2O for **2·sol**) and X-ray crystallography (1 MeOH and 3 H_2O for **1·sol** and 3 H_2O for **2·sol**); however they are still within the limits of detection of each technique. Moreover, the amounts of solvent molecules detected by thermogravimetric and elemental analyses may be disturbed by the inevitable evolution of the sample composition during the sample preparation stage. Thus, in this manuscript, the amount of solvent molecules with the chemical formula of $[Fe(3\text{-bpp})_2](ClO_4)_2{\cdot}2.5H_2O{\cdot}MeOH$ (**1·sol**) and $[Fe(3\text{-bpp})_2](ReO_4)_2{\cdot}3H_2O$ (**2·sol**) is determined based on the most reliable X-ray crystallography technique (*vide infra*).

Additionally, it should be noted that the desolvation is accompanied by a colour change from dark red for the solvated forms to orange-yellow when heated to 120 °C for the desolvated forms. The yellow powder remains unchanged after 2 hours at room temperature for **1** but turns back to red for **2** (ESI, Fig. S2 and S3†). In order to understand the causes of colour changes, infrared (IR) and ultraviolet-visible-near infrared (UV-Vis-NIR) spectroscopy studies were performed at room temperature for the different phases (ESI, Fig. S4 and S5†).

The IR spectra in KBr of **1·sol** and **2·sol** are similar (ESI, Fig. S4†) with characteristic absorption peaks of water molecules (intense broad peaks around 3500 cm^{-1} and weak sharp peaks at 1640 cm^{-1}), the 3-bpp ligand (broad

peaks in the 3400–2500 cm^{-1} range and numerous peaks in the 1600–500 cm^{-1} "fingerprint" region) and the anions (perchlorate in **1·sol** – two intense peaks with maxima around 1100 and 620 cm^{-1}, and perrhenate in **2·sol** a single intense peak at ca. 900 cm^{-1}). Interestingly, the IR spectra of both samples after 24 hours of storage in air under ambient conditions (T = 25 °C, relative humidity 40 ± 5%) indicate a decrease of [ν(O–H)] and [γ(O–H)] absorption bands for **1·sol**, which is a consequence of sample desolvation during storage, while **2·sol** is stable in air. Moreover, both samples after 2 hours of heating at 120 °C are almost completely desolvated which is inferred from the lack of characteristic water absorption peaks after such a thermal treatment, in agreement with TGA analysis.

Complementary studies of solid-state UV-Vis-NIR spectra of **1·sol** and **2·sol** for pristine, ambient condition stored and desolvated forms gave better insight into the spin state of the Fe(II) centre for each phase (ESI, Fig. S5†). High-spin octahedral Fe(II) complexes are known to have one low-intense broad spin-allowed d–d transition ($^5T_{2g} \rightarrow {}^5E_g$) in the Vis/NIR region, while low-spin octahedral Fe(II) complexes are characterised by two intense bands from $^1A_{1g} \rightarrow {}^1T_{2g}$ and $^1A_{1g} \rightarrow {}^1T_{1g}$ transitions in the UV/Vis region.[1] The absorption spectra for both fresh **1·sol** and **2·sol** are very similar with a low intensity broad metal-to-ligand charge transfer (MLCT) band in the NIR range (I) with a maximum of about 800 nm, several strong visible light absorption bands (II) with maxima at around 410, 460, 535 and 620 nm, and two intense π–π* ligand bands in the UV region (III) with maxima at 250 and 310 nm. Spectra of **1·sol** and **2·sol** are in agreement with the intense colour of crystals. Interestingly, after 1 day of storage under ambient conditions, **1·sol** shows a decrease in absorption bands around 535 nm (consisting of MLCT and 3-bpp ligand-localized transitions) and a slight increase in the broad absorption band in the NIR region, indicating a change of the local environment of Fe(II) centres, probably correlated with the slow conversion of LS to HS spin state Fe(II) centres. Concerning **2·sol**, no changes were observed after 24 h hours of storage under ambient conditions, which proves the durability of the material. Heating the samples at 120 °C resulted in a significant reduction in the intensity of all bands in the II range and the appearance of new bands with a maximum above 1000 nm ($^5T_{2g} \rightarrow {}^5E_g$ d–d transition), witnessing the decrease of the LS state in favour of the HS state of Fe(II) at room temperature.

In order to better understand the solid-state optical spectra of **1·sol** and **2·sol** and their evolution during the desolvation process, additional quantum chemical calculations (the single point DFT and TD-DFT calculations) were performed for $[Fe(3\text{-}bpp)_2]^{2+}$ units of **1·sol** and **2·sol** and the HS state reference system of $[Fe(3\text{-}bpp)_2][Au(CN)_2]_2{\cdot}2H_2O$[13a] (see the ESI† for more details). First of all, these studies confirmed a low spin state of **1·sol** and **2·sol**, which can be easily identified from the spin unrestricted energy level diagrams and related molecular orbitals (ESI, Fig. S8 and S9†). Moreover, the ground state to the lowest 100 electronic excited states were calculated with oscillator strength magnetic moment and constituting molecular orbitals, allowing to calculate absorption spectra for all systems (ESI, Fig. S7†). The calculated spectra of **1·sol** and **2·sol** are very similar to each other with several absorption bands consisting of LMCT and d–d transition ($^1A_{1g} \rightarrow {}^1T_{2g}$ and $^1A_{1g} \rightarrow {}^1T_{1g}$) in combination with MLCT and 3-bpp ligand-localized transitions. The spectrum of the HS state reference system is different with mainly MLCT and 3-bpp ligand-localized transitions, and d–d transition ($^5T_{2g} \rightarrow {}^5E_g$) in the lower energy region. Moreover, the calculated spectra are shifted by ca. 200 nm in relation to the experimental spectra due to the applied single-point DFT calculation method, which despite omitting the presence of anions and solvent molecules and the periodicity of the structure in the solid phase, still well reproduce the experimental spectra.

As a summary, all of these studies are consistent and provide a unified image of the processes occurring in **1·sol** and **2·sol** during desolvation. Both fresh compounds contain low-spin Fe(II) complexes, hence the colours observed are dark red at 20 °C. When stored at room temperature, **1·sol** spontaneously loses most of the solvent molecules and turns to orange, while **2·sol** remains stable in this condition. A complete desolvation can be achieved by heating the samples at 120 °C and their colours evolve to yellow and orange for **1** and **2**, respectively. This effect is associated with spin crossover as evidenced by UV-Vis spectrometry. Both compounds clearly show different thermal behaviours which we have investigated further by magnetometry (*vide infra*).

X-ray crystal structure analysis

The crystal structures of **1·sol** and **2·sol** were determined by single-crystal X-ray diffraction measurements. For **1·sol**, being more sensitive to desolvation under ambient conditions, data collection was performed at 90 and 250 K and 250 K for **2·sol**. Both compounds crystallize in the triclinic space group $P\bar{1}$, and their crystallographic parameters are listed in ESI, Table S1.† The asymmetric units of both complexes are almost identical (Fig. 1) and consist of the Fe(II) ion coordinated by two 3-bpp organic ligands, two ClO_4^- and 2.5 water molecules and disordered methanol in the case of **1·sol** or two ReO_4^- counterions and three water molecules in the case of **2·sol**. The [FeN_6] units have a pseudo-octahedral geometry in which each Fe(II) ion is coordinated by six nitrogen atoms belonging to two pyridine (py) and four pyrazole (pyr) groups. The two 3-bpp ligands are in the meridional positions of the distorted octahedron. This distortion is generally observed due to the low mean values of N_{py}–Fe–N_{pyr} angles within 3-bpp ligands of 79.2(2)° and 79.5(2)° for **1·sol** and **2·sol**, respectively (ESI, Table S2†). Furthermore, this deformation is also illustrated by a slight difference in the average Fe–N_{py} and Fe–N_{pyr} bond lengths: 1.926(5) and 1.954(5) Å for **1·sol**, and 1.924(5) and 1.962(4) Å for **2·sol**. Mean Fe–N distances (1.944(5) and 1.949(5) Å for **1·sol** and **2·sol**, respectively) are consistent with the low-spin state of Fe(II).[1a] Calculations of the distortion parameters using Octadist give Σ = 94.31°, Θ = 307.65° and ξ = 0.076 Å for **1·sol** and Σ = 91.93°, Θ = 30.91° and ξ = 0.100 Å for **2·sol**,[23] indicating a slightly more distorted octahedron in **1·sol** than in **2·sol**. This may indicate that the Fe(II) centre in **1·sol** is more prone to experience the LS to HS SCO than in **2·sol**. This observation is in line with the conclusions drawn from the UV-Vis-NIR spectroscopy of fresh samples. At this point it should be noted that the structural parameters related to the complexes [$Fe(3\text{-}bpp)_2$] of both materials are very similar to previously described low-spin state phases of [$Fe(3\text{-}bpp)_2$]X_2·nH_2O (X = Cl, Br and I),[10,18i] [$Fe(3\text{-}bpp)_2$]$(BF_4)_2$·nH_2O,[10] [$Fe(3\text{-}bpp)_2$]$(CF_3SO_3)_2$·nH_2O,[10] and [$Fe(3\text{-}bpp)_2$]$(NCX)_2$·nH_2O (X = S and Se).[10a,15] However, the parameters describing anion environments vary considerably. The average Cl–O and Re–O distances are 1.409(13) and 1.712(6) Å for **1·sol** and **2·sol**, respectively, and the ClO_4^- anions, even at 90 K, are much more disordered than ReO_4^- ones at 250 K.

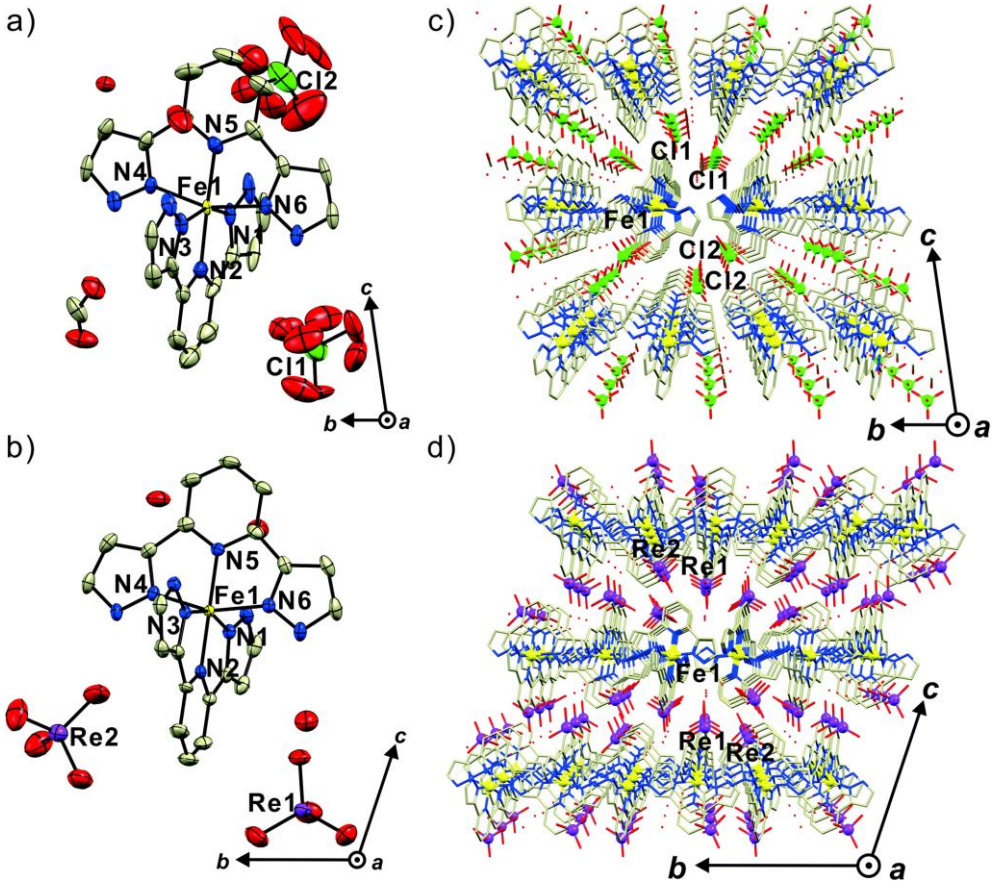

Fig. 1 *Crystal structures of **1·sol** and **2·sol**. Asymmetric units of **1·sol** (a) and **2·sol** (b) with selected atom labelling. Thermal ellipsoids with 50% probability are shown. Packings along the crystallographic a-axis for **1·sol** (c) and **2·sol***

(d). Legend to all figures: C – grey, Cl – green, Fe – yellow, N – blue, O – red, and Re – violet. For clarity, hydrogen atoms have been omitted in all figures.

Crystal packings of **1·sol** and **2·sol** along the crystallographic *a*-axis are shown in Fig. 1. It is noteworthy to mention that both packings are comparable. The layers of Fe(II) complexes lie in the *ab*-plane and are well separated by alternating layers of anions and solvent molecules. Interestingly, the alternating anionic layer of **1·sol** contains only one of two types of perchlorates (Cl1 or Cl2) – Fig. 1c, while **2·sol** consists of both types of perrhenates simultaneously (Re1 and Re2) – Fig. 1d. The layered arrangement of elements in **1·sol** and **2·sol** is the result of the presence of extensive π–π interactions between $[Fe(3\text{-bpp})_2]^{2+}$ entities (Fig. 2a and b), anion–π interactions involving perchlorates/perrhenates and 3-bpp ligands and σ···π interactions between solvent molecules and 3-bpp ligands (Fig. 2c and d), and hydrogen bond networks including 3-bpp ligands, solvent molecules and anions (ESI, Fig. S10†). Each $[Fe(3\text{-bpp})_2]^{2+}$ unit of **1·sol** and **2·sol** interacts *via* parallel-displaced and T-shaped π–π interactions with four adjacent Fe(II) complexes to form two-dimensional layers in the ab-plane (Fig. 2a and b). The average distances between the adjacent pyrazole mean planes (the parallel-displaced π–π interaction distances) are 3.377(2) and 3.575(2) Å for **1·sol** and **2·sol**, respectively. Meanwhile, the average lengths between the pyrazole ring centroids and the hydrogen atoms directly above them (the T-shaped π–π interaction distances) are 2.951(2) and 2.800(2) Å for **1·sol** and **2·sol**, respectively. These relatively small distances indicate the existence of strong π–π stackings, contributing significantly to the stabilization of the overall structures of **1·sol** and **2·sol**. Additionally, the medium-strength anion–π interactions between the lone pairs in the oxygen atoms of XO_4^- anions and pyridine rings of the 3-bpp ligands with the average distance between the pyridine rings centroids and the oxygen atoms directly located above them of 3.029(2) and 3.169(2) Å for **1·sol** and **2·sol** (Fig. 2c and d), respectively, and the intermediate-strength σ···π interactions between the hydrogen atoms of solvent molecules and the pyridine rings of 3-bpp ligands with average distances of 3.337(2) and 3.370(2) Å for **1·sol** and **2·sol**, respectively, also actively participate in the stabilization of **1·sol** and **2·sol**. Furthermore, one-dimensional hydrogen bond networks along the a-direction (for anionic layer with Cl1) or the b-direction (for anionic layer with Cl2) for **1·sol**, and the local hydrogen bond networks for **2·sol** can be recognized (ESI, Fig. S6†), in which each $[Fe(3\text{-bpp})_2]^{2+}$ entity of **1·sol** interacts through N_{pyr}–H···O_{ClO4} and N_{pyr}–H···O_{water} connections at a distance of 2.952(2) and 2.697(2) Å, respectively, while each $[Fe(3\text{-bpp})_2]^{2+}$ unit of **2·sol** interacts via N_{pyr}–H···O_{ReO4} and N_{pyr}–H···O_{water} bonds at a distance of 2.730(2) and 2.747(2) Å, respectively. Moreover, the mean hydrogen bond lengths between the solvent molecules are 2.763(2) and 2.861(2) Å for **1·sol** and **2·sol**, respectively. Interestingly, the hydrogen bonds involving perrhenate are shorter than perchlorate ones.

Unfortunately, under desolvation, crystals lose their crystallinity and the crystal structure of the desolvated phases was not reachable. In order to better understand the desolvation-induced transformation of **1·sol** and **2·sol**, powder X-ray diffraction studies were performed at T = 25 °C in a relative humidity of 40 ± 5% (ESI, Fig. S11†). The perfect match between the measured diffractograms and those calculated from the X-ray structures confirms the homogeneity and phase purity of the pristine samples **1·sol** and **2·sol** used in all experiments. Moreover, diffractograms measured at 10-minute intervals for fresh samples indicate that **1·sol** loses solvent molecules practically after the first scan, reaching the new partially desolvated stable phase within 2 hours, while **2·sol** does not change. These results are in line with TGA and spectroscopic measurements. Finally, powder X-ray diffraction measurements for thermally desolvated samples at 120 °C for 2 hours (**1** and **2**) confirmed that the materials were stable under the experimental conditions (do not return to **1·sol** and **2·sol** phases), and showed lower crystallinity manifested by broadening of the diffraction peaks.

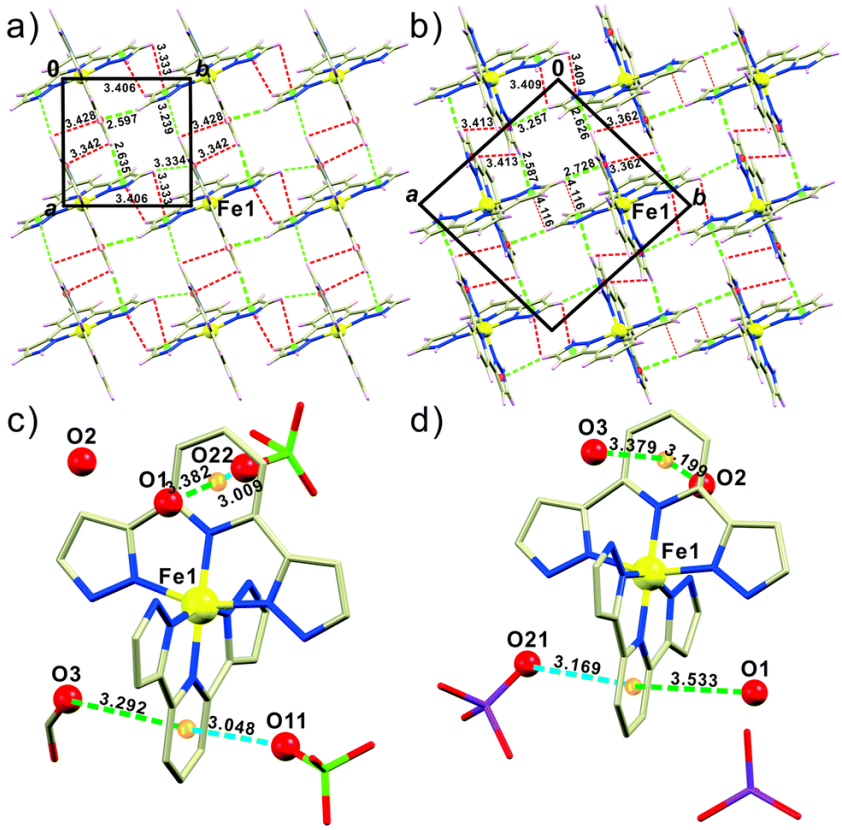

Fig. 2 *The π–π stacking of **1·sol** (a) and **2·sol** (b) located in the ab-plane. The dashed lines represent the parallel-displaced (red lines) and the T-shaped π–π stackings (green lines). The anion–π interactions (blue dashed lines) and the σ···π interactions (green dashed lines) around $[Fe(3\text{-bpp})_2]^{2+}$ entities of **1·sol** (c) and **2·sol** (d). The numbers correspond to the distances between the centroids of the aromatic rings and the hydrogen and oxygen atoms directly located above them.*

Magnetic properties

These experiments were performed using a vibrating sample magnetometer (VSM) under a nitrogen flow with a 2 K min^{-1} sweep rate for polycrystalline samples of **1·sol** and **2·sol**. The magnetic behaviour of **1·sol** in the temperature range (120–370 K) is shown in Fig. 3c. Initially, the product $\chi_M T$ at a low temperature of 120 K (0.1 cm^3 K mol^{-1}) is characteristic of the low-spin state of the Fe(II). With increasing temperature, the magnetic response increases gradually from around 260 K up to 363 K to reach a $\chi_M T$ value of 3.5 cm^3 K mol^{-1}, which corresponds to all Fe(II) centres thermally converted into a high-spin state. After cooling, the magnetic signal gradually decreases until it reaches 0.1 cm^3 K mol^{-1} at 120 K, which means that Fe(II) is in a low-spin state, but it does not follow the initial curve recorded upon warming. The following thermal cycles are superimposed on this second curve, demonstrating the irreversibility of the first warming. The first transition at 340 K can therefore be attributed to the desolvation observed by thermogravimetric analysis (ESI, Fig. S1†). Compound **1** exhibits, after desolvation, a gradual spin transition with $T_{1/2} \approx 210$ K which confirms and complements the earlier observations given by Goodwin et al. for the desolvated sample of $[Fe(3\text{-bpp})_2](ClO_4)_2$.[12e] These results demonstrate, on one hand, that the phenomenon of spin conversion is associated with the complex desolvation process, and on the other hand, that the desolvated compound $[Fe(3\text{-bpp})_2](ClO_4)_2$ (**1**) exhibits a gradual and complete spin crossover. It should be noticed that the derivative curve does not show a symmetric shape. This might be an indication that several sites are switching, as suspected from UV-Vis studies. It is however difficult to conclude without the crystal structure of this desolvated phase. In order to check the stability of this desolvated form, we restudied the magnetic properties of the same sample resulting from the VSM treatment and kept in a container for 5 days. The results shown in Fig. 3c evidence that the two measurements are almost identical which confirms the stability of the desolvated form, when it is stored in the air.

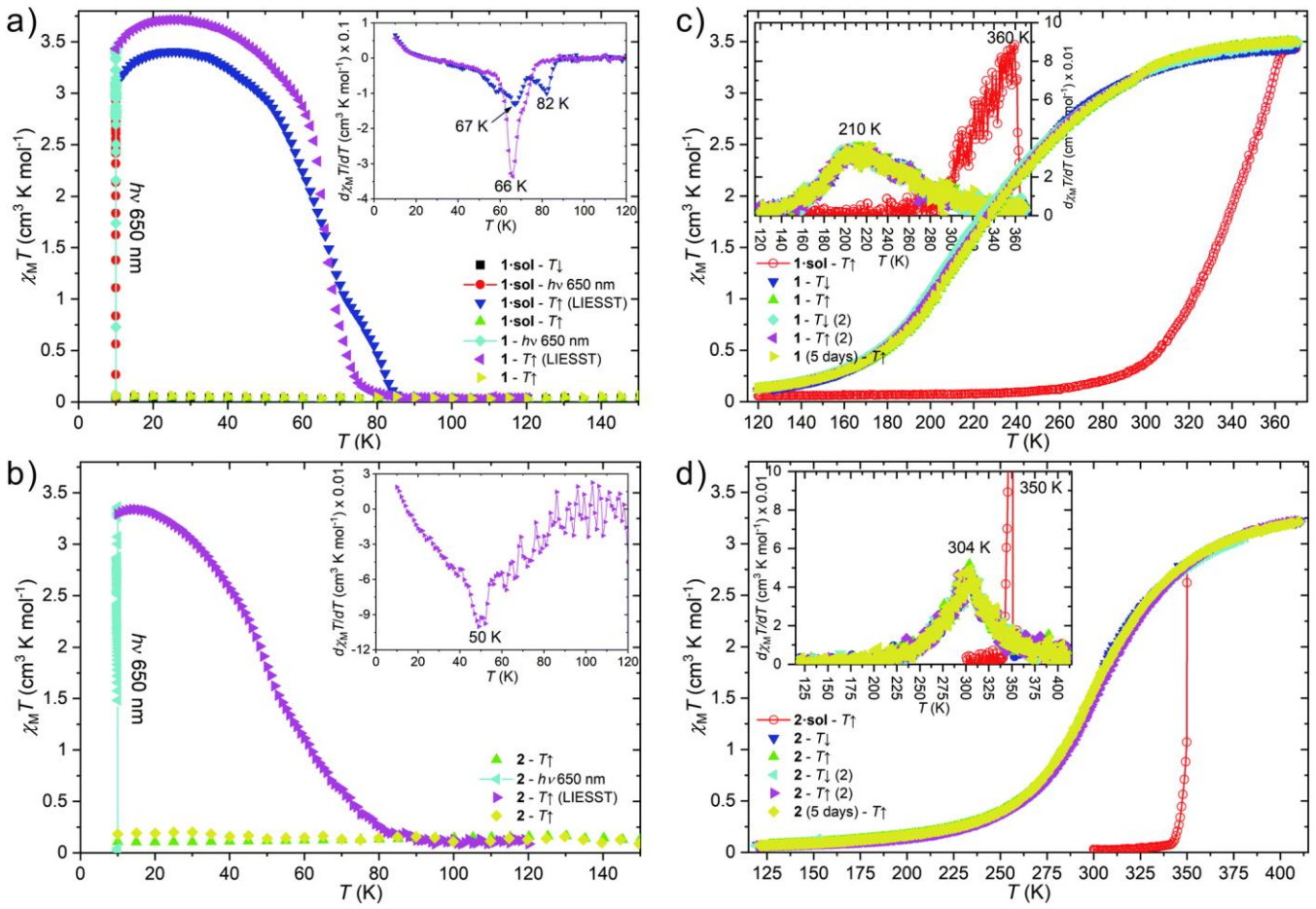

Fig. 3 *Results of magnetic studies and photomagnetic studies at H_{dc} = 10 kOe of pristine (**1·sol** and **2·sol**) and desolvated phases (**1** and **2**). (a) and (b) Temperature dependences of $\chi_M T$ before (black squares), during (red circles) and after photoirradiation with 650 nm light (blue down triangles) of **1·sol**, and after desolvation (green up triangles), during photoirradiation with 650 nm light (light blue left triangles), after photoirradiation (purple right triangles) and after thermal relaxation at 120 K of **1** and **2**. (c) and (d) The temperature dependence of $\chi_M T$ during desolvation (red open circles), two consecutive cooling ($T_{\downarrow}$) and heating ($T_{\uparrow}$) cycles (triangles) and after five days of storing the sample in the air (yellow diamonds). Insets to (c) and (d) contain the first derivatives of the $\chi_M T$ vs. T plots after photoirradiation with 650 nm light for pristine **1·sol** (blue down triangles) and desolvated **1** and **2** (purple right triangles).*

Measurements of the $\chi_M T$ product as a function of temperature were also performed for compound **2·sol** (Fig. 3d). At room temperature, the $\chi_M T$ product (0.05 cm^3 K mol^{-1}) is characteristic of Fe(II) in a low-spin state. An increase in temperature above 350 K causes an abrupt change in the magnetic response followed by a more gradual change upon additional warming. The $\chi_M T$ product reaches 3.2 cm^3 K mol^{-1} at 410 K, which corresponds to Fe(II) centres converted into a high-spin state. As the temperature is lowered, $\chi_M T$ gradually decreases down to 150 K to reach 0.1 cm^3 K mol^{-1}, without overlapping the first warming curve, showing the irreversibility of this first warming. Subsequent cycles show a reproducible gradual conversion. As for **1·sol**, the first heating (red curve) causes a desolvation that changes the magnetic properties of **2·sol**. Compound **2** exhibits a gradual a reversible SCO with a transition temperature $T_{1/2}$ = 304 K. Furthermore, **2** also exhibits good air stability confirmed by magnetic measurement carried out on the material kept in the open thin-walled quartz tube for 5 days.

In conclusion, the analysis of the magnetic properties revealed similar desolvation-assisted SCO effects for both compounds, occurring at 340 and 350 K for **1·sol** and **2·sol**, respectively. After complete desolvation, both systems exhibit a reversible gradual spin conversion with $T_{1/2}$ ≈ 210 K and 304 K for **1** and **2**, respectively. Remarkably, replacing the perchlorate with perrhenate increased the transition temperature by 85 K, moving it slightly above the room temperature region. This implies that the same approach in other SCO systems, based on different organic ligands, could be equally promising. Moreover, the comparison of the $T_{1/2}$ values for the

desolvated **1**, **2** and previously reported $[Fe(3\text{-bpp})_2]X_2$ systems led to the completion of a series of anions, ordered according to increasing temperatures $T_{1/2}$, for the desolvated phases of iron(II) complexes: BF_4^- (175 K)[10a,17] ≈ PF_6^- (177 K)[10] < I^- (204 K)[10b] < **1**–ClO_4^- (210 K) ≈ $NCSe^-$ (231 K)[10a,15] < $[Ag(CN)_2]^-$ (251 K)[12c] ≈ Br^- (252 K)[10] < $[Au(CN)_2]^-$ (291 K)[12c] < **2**–ReO_4^- (304 K), and a discovery of the highest value of $T_{1/2}$ for **2** among the known desolvated $[Fe(3\text{-bpp})_2]$ systems.

Photomagnetic properties

The effect of light irradiation at low temperature was studied on the solvated (**1·sol** and **2·sol**) and desolvated (**1** and **2**) forms at 10 K in the cavity of the SQUID magnetometer coupled by optical fibre to a laser diode emitting at 650 nm light (P = 5 mW cm^{-2}). Fig. 3a shows the study of the photomagnetic properties carried out on the pristine phase of **1·sol**. At 10 K, the sample is initially in the low-spin state. Under the effect of irradiation, the magnetic response increases strongly (ESI, Fig. S12a†), which is interpreted by the population of a metastable high-spin state of Fe(II) centres. In the photostationary state, the $\chi_M T$ product reaches 3.5 cm^3 K mol^{-1}. During the measurement of the relaxation temperature T(LIESST), the magnetic response of compound **1·sol** remains almost unchanged up to 40 K then gradually drops to reach its initial value before photoexcitation. The curve shows a shoulder leading to the estimation of two values of T(LIESST) of 67 and 82 K. This shoulder might come from a partial desolvation occurring during the SQUID ventilation steps necessary to remove atmospheric oxygen and overcome its magnetic response around 50 K (20 minutes purge at room temperature). An attempt was made to study the photomagnetic properties on the desolvated phase (sample from magnetic analysis in VSM). The LIESST effect was observed with T(LIESST) = 66 K (the inset of Fig. 3a). The major difference between the two experiments concerns the shape of the T(LIESST) curves, which is more gradual for the solvated derivative than for the desolvated one. The T(LIESST) of 66 K, close the value observed for the shoulder in **1·sol** supports that this shoulder comes from a partially desolvated sample.

In the case of **2·sol**, no LIESST effect was observed on the solvated compound. An attempt to desolvate the material was performed at 380 K, then another T(LIESST) experiment was performed (Fig. 3b and ESI, Fig. S12b†). After irradiation, almost all molecules are converted to the metastable high-spin state. This irradiation is then stopped and the T(LIESST) is recorded. The T(LIESST) value of 50 K is obtained (the inset of Fig. 3b). The lower T(LIESST) value compared to compound **1** may be due to the fact that the transition temperature $T_{1/2}$ is higher for **2** (304 K) than for **1** (210 K). In accordance with Hauser's inverse energy law and the T(LIESST) database vs. $T_{1/2}$ by Létard, a higher $T_{1/2}$ favours low T(LIESST), for the same family of compounds.[24] This is also supported by slightly lower T(LIESST) values for **1** and **2** than reported ones of 75 K for $[Fe(3\text{-bpp})_2](NCSe)_2$ ($T_{1/2}$ = 231 K),[10a,15] 77 K for $[Fe(3\text{-bpp})_2]Br_2$ ($T_{1/2}$ = 252 K)[10a] and 82 K for $[Fe(3\text{-bpp})_2](PF_6)_2$ ($T_{1/2}$ = 177 K).[10a]

Conclusions

Novel compounds $[Fe(3\text{-bpp})_2](ClO_4)_2{\cdot}2.5H_2O{\cdot}MeOH$ (**1·sol**) and $[Fe(3\text{-bpp})_2](ReO_4)_2{\cdot}3H_2O$ (**2·sol**) were synthesised as a result of self-assembly of Fe(II) with 3-bpp in the presence of perchlorate and perrhenate anions for **1·sol** and **2·sol**, respectively. Fresh compound **1·sol** is susceptible to partial desolvation in air at room temperature, while **2·sol** is air stable. Moreover, both samples after thermal treatment at 120 °C were completely desolvated and could be stored under ambient conditions for a long time without loss of quality. All desolvation processes are accompanied by a colour change from dark red to yellow, and the evolution of IR and UV-Vis-NIR spectra suggests the occurrence of a desolvation-assisted process. X-ray diffraction studies have shown that the structures of both pristine materials are similar and consist of layers of complex cations $[Fe(3\text{-bpp})_2]^{2+}$ separated by solvent molecules and charge-compensating XO_4^- anions (X = Cl, **1·sol** and Re, **2·sol**). All of these building blocks are linked by complex networks of π–π, anion–π and σ···π interactions, and hydrogen bonds. Magnetic measurements indicate that **1·sol** and **2·sol** show desolvation-assisted SCO from the low-spin (LS, S = 0) to high-spin (HS, S = 2) state at 340 and 350 K, respectively, followed by a reversible gradual spin conversion with $T_{1/2}$ ≈ 210 and 304 K for **1** and **2**, respectively. Interestingly, the 304 K transition temperature for **2** is the highest value among the established desolvated $[Fe(3\text{-bpp})_2]$ systems. Finally, photomagnetic studies

confirmed the LIESST phenomenon with *T*(LIESST) = 82 K and 66 K for **1·sol** and **1** phases, respectively. This strongly differs from the perrhenate derivative for which the LIESST effect is exclusively observed for the desolvated sample **2** with *T*(LIESST) ≈ 50 K. This is the first observation of the photomagnetic effect in a perrhenate-based spin crossover system, an effect that is switched on by desolvation.

Experimental section

Materials

Reagents were purchased from commercial sources (Sigma-Aldrich and Alfa Aesar) and used without further purification. The 2,6-di-(1*H*-pyrazol-3-yl)pyridine ligand (3-bpp) was prepared according to a literature procedure.[25]

Caution! We did not encounter any problems during our studies; nevertheless, the perchlorate salt compounds are potentially explosive and should be handled with care.

Synthesis of $[Fe(3\text{-}bpp)_2](ClO_4)_2\cdot 2.5H_2O\cdot MeOH$ (1·sol) and $[Fe(3\text{-}bpp)_2](ReO_4)_2\cdot 3H_2O$ (2·sol)

The complexes **1·sol** and **2·sol** were obtained by following the same procedure in a nitrogen atmosphere: solid $FeCl_2\cdot 4H_2O$ (20 mg, 1 mmol) was added to a 6 ml methanol solution of 3-bpp ligand (42.2 mg, 2 mmol), resulting in the formation of a dark red clear solution. After a few minutes of stirring, a methanol solution of $[Fe(3\text{-}bpp)_2]Cl_2$ was treated with 6 ml of an aqueous solution of $NaClO_4$ (24.5 mg, 2 mmol) or $KReO_4$ (57.9 mg, 2 mmol) for **1·sol** and **2·sol**, respectively. The resulting dark red solution was allowed to evaporate slowly at room temperature, forming dark red crystals. After two weeks, both products were collected. Pristine crystals of **1** have the tendency to lose methanol spontaneously in air, which is associated with the colour change from dark red to orange, thus, it is recommended to not let the solution dry completely and investigate. The average yield is around 75% (50 mg) for **1·sol** and 90% (90 mg) for **2·sol**. Elemental analysis calculated (%) for $C_{23}H_{25.5}Cl_2FeN_{10}O_{10.75}$ (**1·sol**–0.25 H_2O, 740.8 g mol^{-1}): C, 37.29; H, 3.47; N, 18.91; found: C, 37.38; H, 3.74; N, 18.91. Elemental analysis calculated (%) for $C_{22}H_{23}FeN_{10}O_{10.5}Re_2$ (**2·sol**–0.5 H_2O, 1023.8 g mol^{-1}): C, 25.81; H, 2.26; N, 13.68; found: C, 25.83; H, 2.47; N, 13.64.

Single crystal X-ray structure determination

Suitable crystals of **1·sol** and **2·sol** were attached to a MiTeGen microloop using immersion oil under ambient conditions, and were measured on a Rigaku R-AXIS RAPID diffractometer at 90 K for **1·sol** and on a Bruker APEX II diffractometer at 250 K for **2·sol**, using graphite monochromated $Mo_{K\alpha}$ (λ = 0.71075 Å) radiation. Data collection and reduction were performed using a Rigaku RAPID AUTO and a BRUKER SUIT (APEX II) programs for **1·sol** and **2·sol**, respectively. Structures were solved by direct methods using the SHELXL-T package incorporated in the WinGX-2020.1 crystallographic collective package, then refined against F^2 using all data by full-matrix least squares techniques with SHELXL-2014/7 included in the OLEX-2 1.2 software package.[26a,b] Non-hydrogen atoms were refined anisotropically. All hydrogen atoms were positioned with idealized geometry and refined using a riding pattern. The crystal structure of **1·sol** was refined as a two-component twin considering the twin law (1 0 0 0−1 0 0 0−1) with a twin scale factor (BASF) of 0.0090(6). Moreover, in the crystal structure of **1·sol**, both perchlorate anions (Cl1 and Cl2) are disordered at two positions with occupancies of 0.55/0.45 and 0.50/0.50 for Cl1 and Cl2, respectively. A similar behaviour is also observed for solvent molecules of **1·sol**: the water molecules are disordered with occupancies 0.25 for O1A, 0.75 for O1B, and 0.5 for O2, and the ethanol molecule is disordered with occupancy 0.5. All figures were prepared with Mercury 3.9 CCDC visualization software.[26c] Crystal data, data collection, and refinement parameters for **1·sol** and **2·sol** are listed in ESI, Table S2.† CCDC 2073012 and 2073013† contain the supplementary crystallographic data for **1** and **2**, respectively.

Characterization techniques

Elemental analyses (C, H, N) were carried out in a Thermo Fisher FlashEA-1112 microanalyzer with a Mettler Toledo MX5 microbalance. Thermogravimetric analysis (TGA) for the complexes was carried out in a Rigaku Thermo Plus TG8120 apparatus, under an atmosphere of dry N_2 (flow 100 mm min^{-1}) at a heating rate of 2 K min^{-1} over a range from 20 to 400 °C with stabilisation at 25 °C for 1 hour. The infrared (IR) transmission measurements were performed on powdered microcrystals mixed with KBr using a JASCO FT/IR-4100 spectrometer in the range of 4000–400 cm^{-1}. Solid state UV-Vis-NIR diffuse-reflectance spectra for ca. 10 wt% of samples dispersed in $BaSO_4$ were collected with a JASCO V-670 UV-Vis spectrophotometer equipped with an ISN-723 integrating sphere accessory, converted with the Kubelka–Munk function. Powder X-ray diffraction (PXRD) data were recorded on a RIGAKU MiniFleX600 diffractometer equipped with monochromated Cu-Kα radiation (λ = 1.5406 Å), the powder samples were packed into a zero-diffraction plate holder and diffraction patterns were collected over a 2θ range of 3–90° at a scan rate of 10° min^{-1}.

Magnetic measurements

Magnetic measurements were carried out on polycrystalline samples of **1·sol** and **2·sol**, using a vibrating sample magnetometer (VSM) from MicroSense EZ7, equipped with an EV1-LNA temperature controller. Magnetic susceptibility measurements were performed in the temperature range of 120–370 K for **1·sol** and 120–410 K for **2·sol**, respectively, in an applied magnetic field of 10 kOe and a temperature ramp of 2 K min^{-1}. The flow of nitrogen gas was used for temperature control. Samples were placed in thin-walled quartz tubes and immobilised with quartz wool. The magnetic data were corrected from the sample holder and the diamagnetic contributions (using Pascal's constants).[27]

Photomagnetic studies

Photomagnetic measurements were carried out on polycrystals of **1·sol** (0.157 mg) and **2·sol** (0.315 mg) blocked between two transparent polypropylene films. Masses of samples were determined using a microbalance from Mettler Toledo, Mettler ME30 (d = 0.1 mg). Photomagnetic measurements were performed with laser diodes coupled to an optical fibre through the cavity of a MPMS-5 Quantum Design SQUID magnetometer. The standardized procedure for registering the *T*(LIESST) properties was as previously published.[21,24] After cooling slowly to 10 K (in the LS state), samples were irradiated at a given wavelength, and the laser power was adjusted to 5 mW cm^{-2} at the sample surface to minimize and prevent the effect of heating. The magnetization change was followed until the photo-saturation point was reached, then the laser was turned off to stop irradiation. After that, the magnetization was measured in the dark every 1 K in the range of 10–100 K with a temperature ramp of 0.3 K min^{-1} to determine the *T*(LIESST) value given by the extreme of the $\delta\chi_M T/\delta T$ *versus T* curve.[15b,c] In the absence of irradiation, magnetism was also measured over the temperature range of 10 to 150 K to follow the thermal spin transition and obtain a low temperature baseline.

Conflicts of interest

There are no conflicts to declare.

Acknowledgements

The present research was supported by several sources: the CNRS, the University of Bordeaux, the "Agence Nationale de la Recherche" (ANR project BISTA-MAT: ANR-12-BS07-0030-01 ANR project FEMTOMAT: ANR-13-BS04-0002), the "Region Nouvelle Aquitaine", a JSPS Grant-in-Aid for Specially Promoted Research (Grant Number JP15H05697), a Grant-in-Aid for Scientific Research on Innovative Area Soft Crystals (Area No. 2903, JP17H06367), a Grant-in-Aid for Scientific Research(A) (Grant Number JP20H00369), IM-LED LIA (CNRS) and the Algerian General Directorate of Scientific Research and Technological Development (DGRSDT). We acknowledge the Cryogenic Research Center, The University of Tokyo, the Center for Nano Lithography & Analysis, The University of Tokyo supported by MEXT, and the MEXT Quantum Leap Flagship Program (MEXT Q-LEAP) (JPMXS0118068681). K. K. is grateful to a Grant in-Aid for JSPS fellows (Grant Number JP20J20245). O. S. is thankful for JSPS KAKENHI Grant Number JP21K14582.

References

1. (*a*) Spin Crossover in Transition Metal Compounds I-III, in Topics in Current Chemistry, ed. P. Gütlich and H.-A. Goodwin, Springer-Verlag, Berlin, Germany, 2004, vol. 233–235 ; (*b*) Spin-crossover Materials-Properties and Applications, ed. M. A. Halcrow, John Wiley & Sons, Chichester, UK, 2013.
2. (*a*) K. Ridier, Y. Zhang, M. Piedrahita-Bello, C. M. Quintero, L. Salmon, G. Molnár, C. Bergaud and A. Bousseksou, Heat Capacity and Thermal Damping Properties of Spin–Crossover Molecules: A New Look at an Old Topic, Adv. Mater., 2020, 32, 2000987 ; (*b*) K. S. Kumar and M. Ruben, Emerging trends in spin crossover (SCO) based functional materials and devices, Coord. Chem. Rev., 2017, 346, 176–205 ; (*c*) M. D. Manrique-Juárez, S. Rat, L. Salmon, G. Molnár, C. M. Quintero, L. Nicu, H. J. Shepherd and A. Bousseksou, Switchable molecule-based materials for micro- and nanoscale actuating applications: Achievements and prospects, Coord. Chem. Rev., 2016, 308, 395–408 ; (*d*) A. Bousseksou, G. Molnar, L. Salmon and W. Nicolazzi, Molecular spin crossover phenomenon: recent achievements and prospects, Chem. Soc. Rev., 2011, 40, 3313–3335 ; (*e*) O. Kahn and C. J. Martinez, Spin-Transition Polymers: From Molecular Materials Toward Memory Devices, Science, 1998, 279, 44–48.
3. (*a*) S. Brooker, Spin crossover with thermal hysteresis: practicalities and lessons learnt, Chem. Soc. Rev., 2015, 44, 2880–2892 ; (*b*) J. Tao, R.-J. Wei, R.-B. Huang and L.-S. Zheng, Polymorphism in spin-crossover systems, Chem. Soc. Rev., 2012, 41, 703–737 ; (*c*) M. C. Muñoz and J. A. Real, Thermo-, piezo-, photo- and chemo-switchable spin crossover iron(II)-metallocyanate based coordination polymers, Coord. Chem. Rev., 2011, 255, 2068–2093 (*d*) P. Gütlich, V. Ksenofontov and A. B. Gaspar, Pressure effect studies on spin crossover systems, Coord. Chem. Rev., 2005, 249, 1811–1829.
4. (*a*) K. Ridier, A.-C. Bas, Y. Zhang, L. Routaboul, L. Salmon, G. Molnár, C. Bergaud and A. Bousseksou, Unprecedented switching endurance affords for high-resolution surface temperature mapping using a spin-crossover film, Nat. Commun., 2020, 11, 3611 ; (*b*) S. Chorazy, T. Charytanowicz, D. Pinkowicz, J. Wang, K. Nakabayashi, S. Klimke, F. Renz, S. Ohkoshi and B. Sieklucka, Octacyanidorhenate(V) Ion as an Efficient Linker for Hysteretic Two–Step Iron(II) Spin Crossover Switchable by Temperature, Light, and Pressure, Angew. Chem., 2020, 59, 15741–15749 ; (*c*) B. R. Mullaney, L. Goux-Capes, D. J. Price, G. Chastanet, J.-F. Létard and C. J. Kepert, Spin crossover-induced colossal positive and negative thermal expansion in a nanoporous coordination framework material, Nat. Commun., 2017, 8, 1053 ; (*d*) O. I. Kucheriv, V. V. Oliynyk, V. V. Zagorodnii, V. L. Launets and I. A. Gural'skiy, Spin-Crossover Materials towards Microwave Radiation Switches, Sci. Rep., 2016, 6, 38334 ; (*e*) S. Ohkoshi, S. Takano, K. Imoto, M. Yoshikiyo, A. Namai and H. Tokoro, 90-degree optical switching of output second-harmonic light in chiral photomagnet, Nat. Photonics, 2014, 8, 65–71 ; (*f*) T. Liu, H. Zheng, S. Kang, Y. Shiota, S. Hayami, M. Mito, O. Sato, K. Yoshizawa, S. Kanegawa and C. Duan, A light-induced spin crossover actuated single-chain magnet, Nat. Commun., 2013, 4, 2826 ; (*g*) T. Miyamachi, M. Gruber, V. Davesne, M. Bowen, S. Boukari, L. Joly, F. Scheurer, G. Rogez, T. K. Yamada, P. Ohresser, E. Beaurepaire and W. Wulfhekel, Robust spin crossover and memristance across a single molecule, Nat. Commun., 2012, 3, 938 ; (*h*) S. Ohkoshi, K. Imoto, Y. Tsunobuchi, S. Takano and H. Tokoro, Light-induced spin-crossover magnet, Nat. Chem., 2011, 3, 564–569.
5. (*a*) A. J. Fitzpatrick, E. Trzop, H. Müller-Bunz, M. M. Dîrtu, Y. Garcia, E. Collet and G. G. Morgan, Electronic vs. structural ordering in a manganese(III) spin crossover complex, Chem. Commun., 2015, 51, 17540–17543 ; (*b*) S. Hayami, Y. Komatsu, T. Shimizu, H. Kamihata and Y. Lee, Spin-crossover in cobalt(II) compounds containing terpyridine and its derivatives, Coord. Chem. Rev., 2011, 255, 1981–1990 ; (*c*) H.-J. Krüger, Spin transition in octahedral metal complexes containing tetraazamacrocyclic ligands, Coord. Chem. Rev., 2009, 253, 2450–2459 ; (*d*) K. S. Murray, Advances in Polynuclear Iron(II), Iron(III) and Cobalt(II) Spin–Crossover Compounds, Eur. J. Inorg. Chem., 2008, 3101–2121 ; (*e*) G. G. Morgan, K. D. Murnaghan, H. Müller-Bunz, V. McKee and C. J. Harding, A Manganese(III) Complex That Exhibits Spin Crossover Triggered by Geometric Tuning, Angew. Chem., Int. Ed., 2006, 43, 7192–7195 ; (*f*) H. A. Goodwin, Spin Crossover in Cobalt(II) Systems, Top. Curr. Chem., 2004, 234, 23–47 ; (*g*) Y. Garcia and P. Gütlich, Thermal Spin Crossover in Mn(II), Mn(III), Cr(II) and Co(III) Coordination Compounds, Top. Curr. Chem., 2004, 234, 49–62.
6. (*a*) L. J. Kershaw Cook, R. Mohammed, G. Sherborne, T. D. Roberts, S. Alvarez and M. A. Halcrow, Spin state behavior of iron(II)/dipyrazolylpyridine complexes. New insights from crystallographic and solution measurements, Coord. Chem. Rev., 2015, 289–290, 2–12 ; (*b*) G. A. Craig, O. Roubeau and G. Aromí, Spin state switching in 2,6-bis(pyrazol-3-yl)pyridine (3-bpp) based Fe(II) complexes, Coord. Chem. Rev., 2014, 269, 13–31 ; (*c*) I. A. Gass, S. R. Batten, C. M. Forsyth, B. Moubaraki, C. J. Schneider and K. S. Murray, Supramolecular aspects of iron(II) crown-dipyridyl spin-crossover compounds, Coord. Chem. Rev., 2011, 255, 2058–2067 ; (*d*) M. A. Halcrow, Iron(II) complexes of 2,6-di(pyrazol-1-yl)pyridines—A versatile system for spin-crossover research, Coord. Chem. Rev., 2009, 253, 2493–2514.

7. O. Roubeau, Triazole–Based One–Dimensional Spin–Crossover Coordination Polymers, Chem. – Eur. J., 2012, 18, 15230–15244.
8. (*a*) M. G. Reeves, E. Tailleur, P. A. Wood, M. Marchivie, G. Chastanet, P. Guionneau and S. Parsons, Mapping the cooperativity pathways in spin crossover complexes, Chem. Sci., 2021, 12, 1007–1015 ; (*b*) H. Spiering, Elastic Interaction in Spin-Crossover Compounds, Top. Curr. Chem., 2004, 235, 171–195.
9. (*a*) C. W. Sung and B. R. McGarvey, A Study of the Spin−State Transition and Phase Transformation in $[Fe(bpp)_2][CF_3SO_3]_2{\cdot}H_2O$ and $[Fe(bpp)_2][BF_4]_2$ Using Mn^{2+} Electron Spin Resonance, Inorg. Chem., 1999, 38, 3644–3650 ; (*b*) T. Buchen, P. Gütlich, K. H. Sugiyarto and H. A. Goodwin, High–Spin → Low–Spin Relaxation in $[Fe(bpp)_2](CF_3SO_3)_2\ H_2O$ after LIESST and Thermal Spin–State Trapping—Dynamics of Spin Transition Versus Dynamics of Phase Transition, Chem. – Eur. J., 1996, 2, 1134–1138.
10. (*a*) S. Marcén, L. Lecren, L. Capes, H. A. Goodwin and J.-F. Létard, Critical temperature of the LIESST effect in a series of hydrated and anhydrous complex salts $[Fe(bpp)_2]X_2$, Chem. Phys. Lett., 2002, 358, 87–95 ; (*b*) K. H. Sugiyarto, D. C. Craig, A. D. Rae and H. A. Goodwin, Structural, Magnetic and Mössbauer Spectral Studies of Salts of Bis[2,6-bis(pyrazol-3-yl)pyridine]iron(II)—a Spin Crossover System, Aust. J. Chem., 1994, 47, 869–890.
11. (*a*) V. Jornet-Molla, C. Gimenez-Saiz, D. S. Yufit, J. A. K. Howard and F. M. Romero, A Reversible Hydrogen–Bond Isomerization Triggered by an Abrupt Spin Crossover near Room Temperature, Chem. – Eur. J., 2021, 27, 740–750 ; (*b*) M. Clemente-León, E. Coronado, M. C. Giménez-López, F. M. Romero, S. Asthana, C. Desplanches and J.-F. Létard, Structural, thermal and photomagnetic properties of spin crossover $[Fe(bpp)_2]^{2+}$ salts bearing $[Cr(L)(ox)_2]^-$ anions, Dalton Trans., 2009, 8087–8095 ; (*c*) E. Coronado, M. C. Giménez-López, C. Giménez-Saiz and F. M. Romero, Spin crossover complexes as building units of hydrogen-bonded nanoporous structures, CrystEngComm, 2009, 11, 2198–2203.
12. (*a*) V. Jornet-Mollá, C. Giménez-Saiz and F. M. Romero, Synthesis, Structure, and Photomagnetic Properties of a Hydrogen-Bonded Lattice of $[Fe(bpp)_2]^{2+}$ Spin-Crossover Complexes and Nicotinate Anions, Crystals, 2018, 8, 439 ; (*b*) S. A. Barrett and M. A. Halcrow, Anion-dependent spin crossover in solution for an iron(II) complex of a 1H-pyrazolyl ligand, RSC Adv., 2014, 4, 11240–11243 ; (*c*) P. King, J. J. Henkelis, C. A. Kilner and M. A. Halcrow, Four new spin-crossover salts of $[Fe(3\text{-}bpp)_2]^{2+}$ (3-bpp = 2,6- bis [1H-pyrazol-3-yl]pyridine), Polyhedron, 2013, 52, 1449–1456 ; (*d*) S. A. Barrett, C. A. Kilner and M. A. Halcrow, Spin-crossover in $[Fe(3\text{-}bpp)_2][BF_4]_2$ in different solvents – A dramatic stabilisation of the low-spin state in water, Dalton Trans., 2011, 40, 12021–12024 ; (*e*) K. H. Sugiyarto and H. A. Goodwin, Coordination of Pyridine-Substituted Pyrazoles and Their Influence on the Spin State of Iron(II), Aust. J. Chem., 1988, 41, 1645–1663.
13. (*a*) A. Djemel, O. Stefanczyk, M. Marchivie, E. Trzop, E. Collet, C. Desplanches, R. Delimi and G. Chastanet, Solvatomorphism–Induced 45 K Hysteresis Width in a Spin–Crossover Mononuclear Compound, Chem. – Eur. J., 2018, 24, 14760–14767 ; (*b*) N. Paradis, G. Chastanet, F. Varret and J.–F. Létard, Metal Dilution of Cooperative Spin–Crossover Compounds: When Stable and Metastable High–Spin States Meet, Eur. J. Inorg. Chem., 2013, 968–974 ; (*c*) N. Paradis, G. Chastanet and J.–F. Létard, When Stable and Metastable HS States Meet in Spin–Crossover Compounds, Eur. J. Inorg. Chem., 2012, 3618–3624.
14. (*a*) V. Jornet-Molla, C. Gimenez-Saiz, L. Canadillas-Delgado, D. S. Yufit, J. A. K. Howard and F. M. Romero, Interplay between spin crossover and proton migration along short strong hydrogen bonds, Chem. Sci., 2021, 12, 1038–1053 ; (*b*) M. Clemente-León, E. Coronado, M. C. Giménez-López and F. M. Romero, Structural, Thermal, and Magnetic Study of Solvation Processes in Spin-Crossover $[Fe(bpp)_2][Cr(L)(ox)_2]_2{\cdot}nH_2O$ Complexes, Inorg. Chem., 2007, 46, 11266–11276 ; (*c*) A. Bhattacharjee, V. Ksenofontov, K. H. Sugiyarto, H. A. Goodwin and P. Gütlich, Anomalous Spin Transition Observed in Bis(2,6−bis(pyrazol–3−yl)pyridine)iron(II) Thiocyanate Dihydrate, Adv. Funct. Mater., 2003, 13, 877–882.
15. (*a*) C. Baldé, C. Desplanches, F. Le Gac, P. Guionneau and J.-F. Létard, The role of iron(II) dilution in the magnetic and photomagnetic properties of the series $[Fe_x,Zn_{1-x}(bpp)_2](NCSe)_2$, Dalton Trans., 2014, 43, 7820–7829 ; (*b*) C. Baldé, C. Desplanches, P. Gütlich and J.-F. Létard, Effect of the metal dilution on the thermal and light-induced spin transition in $[Fe_x,Mn_{1-x}(bpp)_2](NCSe)_2$: When T(LIESST) reaches $T_{1/2}$, Inorg. Chim. Acta, 2008, 361, 3529–3533 ; (*c*) J. F. Létard, C. Carbonera, E. Courcot and J. S. Costa, A typical example of a photomagnetic study carried out on a spin-crossover material, Bull. Mater. Sci., 2006, 29, 567–571 ; (*d*) K. H. Sugiyarto, M. L. Scudder, D. C. Craig and H. A. Goodwin, Electronic and Structural Properties of the Spin Crossover Systems Bis(2,6-bis(pyrazol-3-yl)pyridine)iron(II) Thiocyanate and Selenocyanate, Aust. J. Chem., 2000, 53, 755–765.
16. K. H. Sugiyarto, W. A. McHale, D. C. Craig, A. D. Rae, M. L. Scudder and H. A. Goodwin, Spin transition centres linked by the nitroprusside ion. The cooperative transition in bis(2,6-bis(pyrazol-3-yl)pyridine)iron(II) nitroprusside, Dalton Trans., 2003, 2443–2448.
17. (*a*) T. Buchen, P. Gütlich and H. A. Goodwin, Non-First-Order Kinetics of the High Spin-Low Spin Relaxation in $[Fe(bpp)_2](BF_4)_2$ after LIESST and Thermal Spin Trapping, Inorg. Chem., 1994, 33, 4573–4576 ; (*b*) K. H. Sugiyarto

and H. A. Goodwin, Lattice trapping of metastable quintet state bis(2,6-bis(pyrazol-3-yl)pyridine)iron(II) bis(tetrafluoroborate), a spin crossover system, and kinetics of the quintet-singlet transformation, Chem. Phys. Lett., 1987, 139, 470–474.

18. (*a*) M. A. Halcrow, I. C. Berdiell, C. M. Pask and R. Kulmaczewski, Relationship between the Molecular Structure and Switching Temperature in a Library of Spin-Crossover Molecular Materials, Inorg. Chem., 2019, 58, 9811–9821 ; (*b*) M. del C. Giménez-López, M. Clemente-León and C. Giménez-Saiz, Unravelling the spin-state of solvated $[Fe(bpp)_2]^{2+}$ spin-crossover complexes: structure–function relationship, Dalton Trans., 2018, 47, 10453–10462 ; (*c*) V. Jornet-Molla, Y. Duan, C. Gimenez-Saiz, Y.-Y. Tang, P.-F. Li, F. M. Romero and R.-G. Xiong, A Ferroelectric Iron(II) Spin Crossover Material, Angew. Chem., Int. Ed., 2017, 56, 14052–14056 ; (*d*) C. Baldé, C. Desplanches, J. F. Létard and G. Chastanet, Effects of metal dilution on the spin-crossover behavior and light induced bistability of iron(II) in $[Fe_x,Ni_{1-x}(bpp)_2](NCSe)_2$, Polyhedron, 2017, 123, 138–144 ; (*e*) V. Jornet-Mollá, Y. Duan, C. Giménez-Saiz, J. C. Waerenborgh and F. M. Romero, Hydrogen-bonded networks of $[Fe(bpp)_2]^{2+}$ spin crossover complexes and dicarboxylate anions: structural and photomagnetic properties, Dalton Trans., 2016, 45, 17918–17928 ; (*f*) G. A. J. Craig, S. Costa, O. Roubeau, S. J. Teat and G. Aromí, Local Coordination Geometry and Spin State in Novel Fe^{II} Complexes with 2,6−Bis(pyrazol–3−yl)pyridine–Type Ligands as Controlled by Packing Forces: Structural Correlations, Chem. – Eur. J., 2012, 18, 11703–11715 ; (*g*) A. Bhattacharjee, J. Kusz, M. Zubko, H. A. Goodwin and P. Gütlich, Synchrotron powder-diffraction study of the spin transition compound $[Fe(bpp)_2](NCS)_2{\cdot}2\ H_2O$ and soft X-ray-induced structural phase conversion, J. Mol. Struct., 2008, 890, 178–183 ; (*h*) E. Coronado, J. R. Galán-Mascarós, M. C. Giménez-López, M. Almeida and J. C. Waerenborgh, Spin crossover Fe^{II} complexes as templates for bimetallic oxalate-based 3D magnets, Polyhedron, 2007, 26, 1838–1844 ; (*i*) M. L. Scudder, D. C. Craig and H. A. Goodwin, Hydrogen bonding influences on the properties of heavily hydrated chloride salts of iron(II) and ruthenium(II) complexes of 2,6-bis(pyrazol-3-yl)pyridine, 2,6-bis(1,2,4-triazol-3-yl)pyridine and 2,2′:6′,2′′-terpyridine, CrystEngComm, 2005, 7, 642–649 ; (*j*) M. C. Giménez-López, M. Clemente-León, E. Coronado, F. M. Romero, S. Shova and J.-P. Tuchagues, Structural Transformations and Magnetic Effects Induced by Solvent Exchange in the Spin Crossover Complex $[Fe(bpp)_2][Cr(bpy)(ox)_2]_2$, Eur. J. Inorg. Chem., 2005, 2783–2787 ; (*k*) E. Coronado, M. C. Giménez-López, C. Giménez-Saiz, J. M. Martínez-Agudo and F. M. Romero, Synthesis, structure and magnetic properties of iron(II), cobalt(II) and nickel(II) complexes of 2,6-bis(pyrazol-3-yl)pyridine and paramagnetic counterions, Polyhedron, 2003, 22, 2375–2380.
19. V. Jornet-Molla, C. Gimenez-Saiz, B. J. C. Vieira, J. C. Waerenborgh and F. M. Romero, Temperature dependence of desolvation effects in hydrogen-bonded spin crossover complexes, Dalton Trans., 2021, 50, 2536–2544.
20. (*a*) S. Decurtins, P. Gutlich, C. P. Kohler, H. Spiering and A. Hauser, Light-induced excited spin state trapping in a transition-metal complex: The hexa-1-propyltetrazole-iron(II) tetrafluoroborate spin-crossover system, Chem. Phys. Lett., 1984, 105, 1–4 ; (*b*) G. Chastanet, M. Lorenc, R. Bertoni and C. Desplanches, Light-induced spin crossover—Solution and solid-state processesConversion de spin photo-induite – Processus en solution et en phase solide, C. R. Chim., 2018, 21, 1075–1094 ; (*c*) J.-F. Létard, Photomagnetism of iron(II) spin crossover complexes—the T(LIESST) approach, J. Mater. Chem., 2006, 16, 2550–2559 ; (*d*) A. Hauser, Light-Induced Spin Crossover and the High-Spin → Low-Spin Relaxation, Top. Curr. Chem., 2004, 234, 155–198.
21. (*a*) G. Chastanet, C. Desplanches, C. Baldé, P. Rosa, M. Marchivie and P. Guionneau, A critical review of the T(LIESST) temperature in spin crossover materials − What it is and what it is not, Chem. Sq., 2018, 2, 2 ; (*b*) J.-F. Létard, L. Capes, G. Chastanet, N. Moliner, S. Létard, J. A. Real and O. Kahn, Critical temperature of the LIESST effect in iron(II) spin crossover compounds, Chem. Phys. Lett., 1999, 313, 115–120 ; (*c*) J.-F. Létard, P. Guionneau, L. Rabardel, J. A. K. Howard, A. E. Goeta, D. Chasseau and O. Kahn, Structural, Magnetic, and Photomagnetic Studies of a Mononuclear Iron(II) Derivative Exhibiting an Exceptionally Abrupt Spin Transition. Light-Induced Thermal Hysteresis Phenomenon, Inorg. Chem., 1998, 37, 4432–4441.
22. (*a*) O. G. Shakirova and L. G. Lavrenova, Spin Crossover in New Iron(II) Coordination Compounds with Tris(pyrazol-1-yl)Methane, Crystals, 2020, 10, 843 ; (*b*) L. G. Lavrenova and O. G. Shakirova, Spin Crossover and Thermochromism of Iron(II) Coordination Compounds with 1,2,4−Triazoles and Tris(pyrazol–1−yl)methanes, Eur. J. Inorg. Chem., 2013, 670–682 ; (*c*) M. B. Bushuev, L. G. Lavrenova, Y. G. Shvedenkov, A. V. Virovets, L. A. Sheludyakova and S. V. Larionov, Synthesis and study of Iron(II) perrhenate complexes with 4-propyl-1,2,4-triazole exhibiting $^1A_1 \rightleftarrows {}^5T_2$ spin transition, Russ. J. Inorg. Chem., 2007, 52, 46–51.
23. R. Ketkaew, Y. Tantirungrotechai, P. Harding, G. Chastanet, P. Guionneau, M. Marchivie and D. J. Harding, OctaDist: a tool for calculating distortion parameters in spin crossover and coordination complexes, Dalton Trans., 2021, 50, 1086–1096.
24. (*a*) J. F. Létard, P. Guionneau, O. Nguyen, J. Sánchez Costa, S. Marcén, G. Chastanet, M. Marchivie and L. Goux-Capes, A Guideline to the Design of Molecular–Based Materials with Long–Lived Photomagnetic Lifetimes, Chem.

– Eur. J., 2005, 11, 4582–4589 ; (*b*) A. Hauser, A. Vef and P. Adler, Intersystem crossing dynamics in Fe(II) coordination compounds, J. Chem. Phys., 1991, 95, 8710–8717.

25. Y. Lin and S. A. Lang, Novel two step synthesis of pyrazoles and isoxazoles from aryl methyl ketones, J. Heterocycl. Chem., 1977, 14, 435–347.
26. (*a*) G. M. Sheldrick, Crystal structure refinement with SHELXL, Acta Crystallogr., Sect. C: Struct. Chem., 2015, 71, 3–8 ; (*b*) O. V. Dolomanov, L. J. Bourhis, R. J. Gildea, J. A. K. Howard and H. Puschmann, OLEX2: a complete structure solution, refinement and analysis program, J. Appl. Crystallogr., 2009, 42, 339–341 ; (*c*) C. F. Macrae, I. J. Bruno, J. A. Chisholm, P. R. Edgington, P. McCabe, E. Pidcock, L. Rodriguez-Monge, R. Taylor, J. van de Streek and P. A. Wood, Mercury CSD 2.0 – new features for the visualization and investigation of crystal structures, J. Appl. Crystallogr., 2008, 41, 466–470.
27. O. Kahn, Molecular Magnetism, VCH, New York, 1993, ch. 1.